Electro-optic modulators based on hybrid plasmonic micro-ring-disk resonators with femtojoule switching energy

Dimitrios C. Zografopoulos[1] · **Mohamed A. Swillam**[2] · **Romeo Beccherelli**[1]

Abstract An electro-optic modulator based on hybrid plasmonic micro-ring-disks with submicron radii is designed and rigorously investigated via the finite-element method. The device is based on the conductor-gap-silicon hybrid plasmonic platform and utilizes an embedded electro-optical polymer to control the resonant wavelengths of micro-ring-disk resonators. Such elements combine the easier fabrication of microdisks with the lower capacitance of microring resonators and provide high modulation depths, low insertion losses, and energy consumption around 1 fJ/bit. Finally, an add-drop filter configured in a 2×2 switching matrix is presented and its performance is preliminary assessed.

1 Introduction

Not limited by the diffraction limit inherent to integrated photonic platforms based on purely dielectric waveguides, plasmonic circuits offer the possibility for dense integration by guiding light at sub-wavelength scales, in the form of surface light waves at the interface between metals and dielectrics. The miniaturization of the overall footprint of plasmonic architectures is the key element toward the merging between electronics and photonics in new generation integrated chips that benefit from the best features of both worlds, namely dense integration with high bandwidth and low latency [1].

Indispensable components in integrated chips are optical modulators, which convert the electrical information signal into optical pulses, and switches that control the flow of information through the circuit channels. When it comes to plasmonic-based devices, the employment of electro-optically responsive materials provides promising solutions toward the implementation of efficient modulators, by utilizing the same metallic parts as both light waveguides and electrical contacts and by maximizing light-matter interaction between the electro-optic material and the propagating optical signal [2, 3]. Various physical phenomena have been thus far exploited, such as the carrier concentration change effect thin transparent oxide layers [4], the Pockels effect in $\chi^{(2)}$ nonlinear polymers [5, 6], or the electro-optic tuning of liquid crystalline materials [7–9].

In particular, the Pockels effect in electro-optic polymers (EOP) offers a powerful alternative for the implementation of tunable integrated components. The field-effect actuation of EOP devices ensures high modulation bandwidths, stemming from the ultrafast molecular polarizability, and low power requirements. Such favorable properties have been extensively demonstrated in EOP-tunable components in the silicon-organic hybrid (SOH) platform [10, 11]. As far as integrated plasmonics are concerned, EOP have been shown promising in various configurations, e.g., dielectric-loaded ring resonators [12],

✉ Dimitrios C. Zografopoulos
dimitrios.zografopoulos@artov.imm.cnr.it

1 Consiglio Nazionale delle Ricerche, Istituto per la Microelettronica e Microsistemi (CNR-IMM), 00133 Rome, Italy

2 Department of Physics, School of Science and Engineering, The American University in Cairo, New Cairo 11835, Egypt

metal-insulator-metal (MIM) amplitude [6, 13] or phase modulators [5], MIM filters [14–16], hybrid waveguides and resonators [17, 18], and conductor-gap-silicon (CGS) plasmonic in directional coupler [19] or resonant configurations [20–22]. Among these plasmonic approaches, the CGS hybrid plasmonic platform [23–28] overall offers a series of important advantages: (1) interfacing with Si photonic waveguides with very high coupling efficiencies, as demonstrated in [23], (2) potential for CMOS-compatibility, (3) lower propagation/insertion losses and much higher resonator quality factors with respect to purely plasmonic, e.g., MIM, approaches, and (4) significantly tighter light confinement and hence reduced device footprint with respect to all-dielectric platforms, e.g., Si or III/V-photonics.

In this work, we present the design of a plasmonic modulator implemented in the CGS platform and based on resonating micro-ring-disks, namely the combination of sub-micron silicon microdisks with plasmonic rings. Compared to microring resonators, this approach relaxes the fabrication complexity and eliminates any scattering losses in the interior surface of Si microrings. In the same time, it features much lower overall system capacitance and thus energy consumption than microdisk resonators [21], without compromising the modulation performance. Moreover, an n-doped Si rib is introduced in the design, which offers a natural option for the electrical connectorization of the device, and its effect is rigorously taken into account.

Initially, the properties of the single resonating elements are investigated via the finite-element method, leading to an optimal selection of geometrical parameters that yields favorable performance. Then, by side coupling the micro-ring-disk to a CGS bus waveguide, an electro-optic modulator is demonstrated, which features small footprint, high modulation depth, low insertion losses, high operation speeds and very low capacitance, leading to femtojoule/bit switching energies. Finally, the modulator's performance is also preliminarily assessed in a four-port switching matrix configuration.

2 Electro-optic integrated hybrid plasmonic modulator

2.1 Properties of the single micro-ring-disk hybrid plasmonic resonator

The proposed plasmonic modulator is based on the micro-ring-disk resonating element schematically depicted in Fig. 1. Starting from a SOI wafer, which is typically flat to the atomic scale, a Si microdisk with radius R_o is patterned. The thickness of the silicon layer is $h_{Si} = 300$ nm.
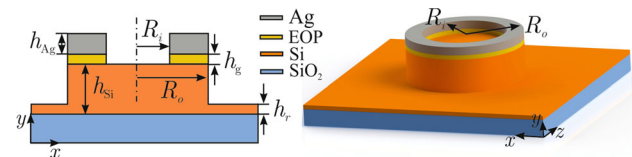

Fig. 1 Schematic layout of the proposed electro-optic micro-ring-disk plasmonic resonator. A silicon microdisk is patterned on a silicon-on-insulator wafer, not fully etched in order to provide for a native electrode for the RF connectorization of the modulator. On top, a silver micro-ring is defined, separated by the silicon disk via a thin layer of an electro-optic polymer

However, Si is not fully etched, such that the remaining layer of thickness $h_r = 30$ nm may serve as one of the two electrical connections to the micro-ring-disk, via which the modulating voltage is applied to the resonator, as it will be explained in the end of this Section. On top of the micro-disk, a silver microring of thickness $h_{Ag} = 100$ nm and internal radius R_i is defined, separated from the Si micro-disk via a thin layer of electro-optic polymer (EOP), whose thickness is equal to $h_g = 30$ nm. The deposition of the EOP layer can be performed by spin-coating, which is widely employed in the fabrication of silicon- or plasmonic-based EO modulators [29]. The etching of the final features is possible via, e.g., e-beam lithography, as in the EO plasmonic modulators based on the dielectric-loaded platform demonstrated in [12]. Once the final structure is fabricated, a poling field is applied in order to align the chromophores in the host polymer and induce the necessary nonlinear response. The poling process, which takes place at an elevated temperature close to the glass-transition point of the host polymer, is preferably done in an oxygen-free environment, e.g., nitrogen, in order to avoid oxidization of the silver layers and oxygen diffusion that can damage the electro-optic chromophores [30].

The combination of a Si microdisk with a plasmonic microring eliminates the scattering in the interior walls of Si microrings, while keeping low the overall capacitance of the structure, which is mainly defined by the dimensions of the Ag microring, thus reducing the required modulating switching energy, as it will be demonstrated. The substrate is silica, considered to be thick enough in order to optically isolate the plasmonic circuit from the bulk of the Si wafer.

The resonant wavelengths λ_r of the micro-disk-ring depend mainly on its external dimension, i.e., the external radius R_o, which can be adjusted such that the structure resonates close to the technologically relevant wavelength of 1.55 μm [20, 21]. In order to calculate the resonant wavelengths, we employ an eigenmode analysis implemented in the finite-element method [31]. The permittivity of Ag is equal to $\varepsilon_{Ag} = -126 - j2.86$, the refractive index of silica is $n_{sil} = 1.444$, while that of the EOP is $n_p = 1.83$, which corresponds to DLD-164, a material with high
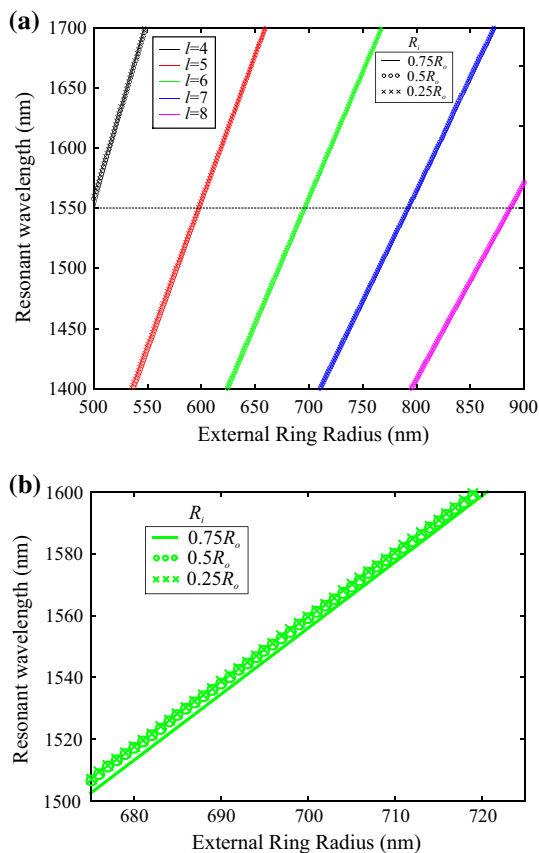
Fig. 2 **a** Resonant wavelengths of the micro-disk-ring resonator as a function of the external ring radius R_o for three values of the internal ring radius R_i and for an azimuth number l ranging from 4 to 8. **b** *Zoomed graph* for the $l = 6$ mode around the telecom important wavelength of 1.55 μm

electro-optic coefficient $r_{33} = 180$ pm/V (measured in the device), recently employed in state-of-the-art EOP-based plasmonic modulators [13]. The Si refractive index is $n_{Si} = 3.48 + \Delta n_{fc}$, where Δn_{fc} is the index modulation, considering that Si is doped in order to lower its resistivity and thus increase the bandwidth of the modulator, a
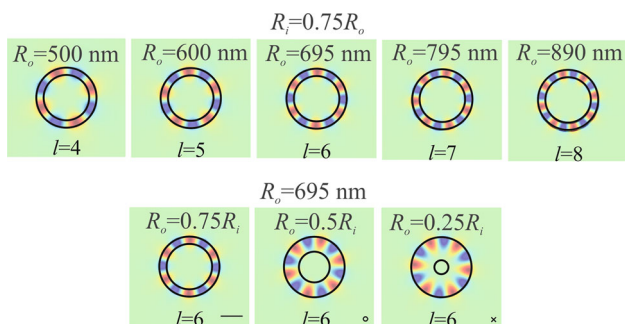

Fig. 3 Profile of the y-component of the electric field at the mid-plane of the EOP layer, for the resonant eigenmodes calculated at $\lambda = 1.55$ μm in Fig. 2. The field profile remains practically undisturbed for $R_i = 0.25R_o$ and $R_i = 0.5R_o$

technique which is typically employed in silicon photonics modulators based on the field effect. Here, we assume that Si is As-doped at a concentration $N_e = 10^{19}$ cm^{-3}, which lowers its resistivity to $\rho = 0.006\,\Omega$/cm, thus yielding a sheet resistance of 2 KΩ/sq for the considered thickness h_r. The resulting free-carrier (FC) modulation is $\Delta n_{fc} \simeq -0.01 - j0.001$ and it has been taken into account in the analysis. It is stressed that although the introduction of free-carrier-induced losses may have a detrimental effect in purely dielectric silicon photonics modulators, in the investigated structure it does not have a notable effect, since the losses of the structure are governed almost exclusively by damping at the Ag/EOP interface.

Figure 2 shows the resonant wavelength for R_o ranging from 500 to 900 nm and considering three cases for the internal radius R_i. The wavelength λ_r is associated with a mode with radial number equal to 1 and an azimuthal number l that varies from 4 to 8 as the dimensions of the resonator become larger. This mode has the largest quality factor, and it is the only one in the wavelength window under study, which can efficiently couple to a bus waveguide, as it will be demonstrated in Sect. 2.2. At certain discrete values of R_o, the λ_r equals the target wavelength of 1.55 μm. The influence of the internal radius value R_i on λ_r is rather limited, as shown also in Fig. 2b, which is a zoomed graph referring to the $l = 6$ resonant mode around 1.55 μm. More specifically, the results are identical for $R_i = 0.25R_o$ and $R_i = 0.5R_o$, while there is a few-nm shift of λ_r for $R_i = 0.75R_o$.

This behavior can be easily understood by inspecting the profile of the y-component of the electric field of the resonant eigenmodes of the system, which is plotted in Fig. 3 for $\lambda_r \sim 1.55$ μm and for various combinations of R_o and R_i. The profiles were calculated at the mid-plane of the EOP
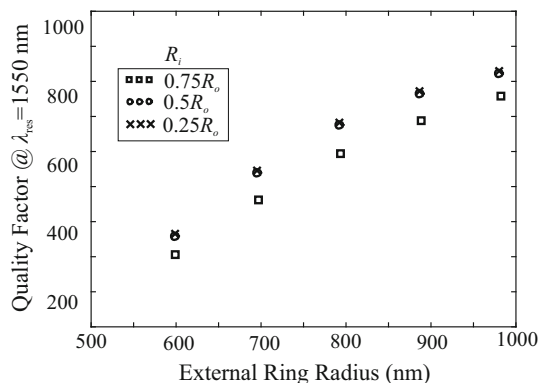
**Fig. 4** Quality factors of the single resonator eigenmodes at $\lambda = 1.55$ μm for $l = 5...9$ for three different R_i values. For $R_i = 0.25R_o$ and $R_i = 0.5R_o$ the quality factors are almost equal. For higher values ($R_i = 0.75R_o$) the resonator becomes more lossy, since the field leaks out from the ring's inner surface, leading to lower values of the quality factor

layer. As the resonator becomes bigger, the azimuthal number of the resonant mode increases, up to $l = 8$ for $R_o = 890$ nm. More interesting, for a given R_o the profiles for $R_i = 0.25R_o$ and $0.5R_o$ do not show any difference, as the electric field is concentrated close to the circumference of the EOP ring layer, indicating that R_i can be increased up to a certain value without compromising the field confinement and, therefore, the quality of the resonator. This is more clearly reflected in the results of Fig. 4, which reports the quality factors Q of the resonant eigenmodes at approximately 1.55 µm. There is no significant variation when increasing R_i from $0.25R_o$ to $0.5R_o$, although a further increase to $0.75R_o$ leads to a reduction of Q as the resonator becomes more leaky toward the interior of the ring structure. Larger structures offer higher Q values, albeit at the expense of larger device footprint and capacitance. Moreover, the slope of the increase of Q for $l > 8$ is reduced, meaning that it is not straightforward to increase arbitrarily Q by simply scaling the device. On the other hand, smaller resonators associated with lower l numbers are more compact, however also more leaky and therefore are expected to be less efficient in tuning. As a balanced solution, here we focus on four configurations corresponding to $R_o = 695$ nm ($l = 6$) and 795 nm ($l = 7$), while R_i takes the values $0.5R_o$ and $0.75R_o$.

In order to assess the tunability of the resonating structures, we modify the polymer index by Δn_p and calculate the corresponding shift of the resonant wavelength. The EOP index modulation stems from the electro-optic effect and equals $\Delta n_p = 0.5n_p^3 r_{33}E_s$, where E_s is the intensity of the applied RF modulating field in the polymer. For a breakdown intensity limit of 100 V/µm, typical of EOP used in the SOH platform, the maximum index modulation is ~ 0.055. Figure 5 investigates into the
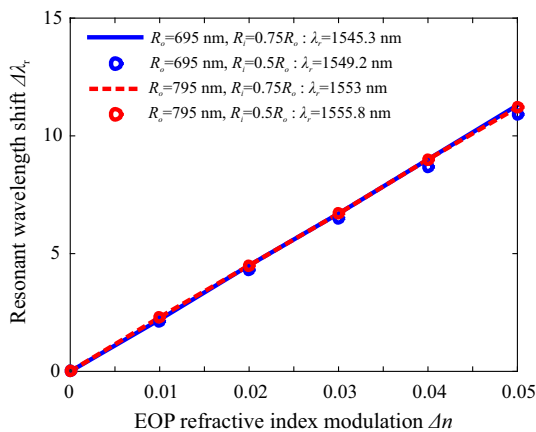
Fig. 5 Shift of the resonant wavelength for four cases under investigation as a function of the modulation of the electro-optic polymer refractive index. In all cases, the tunability obtains almost identical values, around 220 nm/RIU
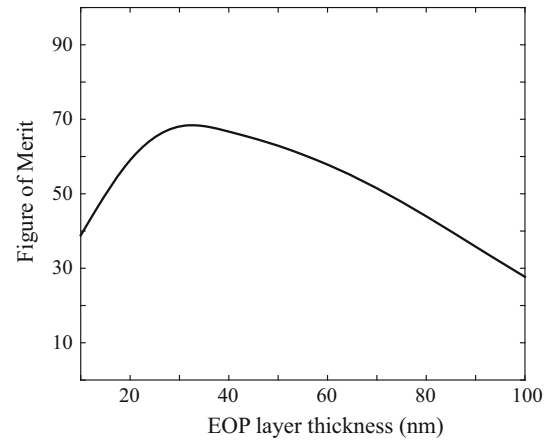

Fig. 6 Figure of merit, defined as $(Q/\lambda_r) \cdot (\Delta\lambda_r/\Delta n_p)$, as a function of the electro-optic polymer layer thickness, calculated for $R_i = 0.75R_o$. The best performance is predicted for a layer thickness of approximately 30 nm
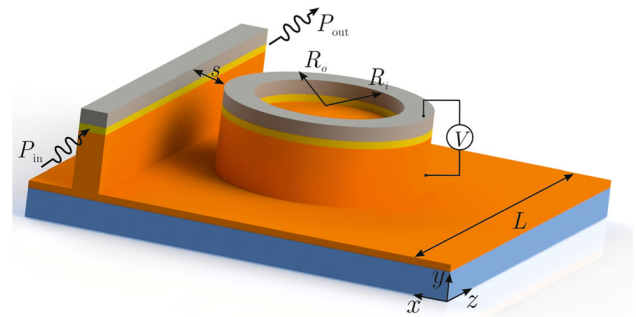
Fig. 7 Schematic layout of the hybrid plasmonic modulator consisting of a conductor-gap-silicon bus waveguide side-coupled with a micro-ring-disk resonator

tunability of the four resonators under study, revealing a linear dependence with a $\Delta\lambda_r/\Delta n_p \simeq 220$ nm/RIU, almost equal in all four cases. Nevertheless, the overall tuning efficiency of the resonator also depends on the quality factor, which is directly associated with the linewidth of the resonances. A relevant figure of merit can be defined as FoM $= (Q/\lambda_r) \cdot (\Delta\lambda_r/\Delta n_p)$ [20], that takes into account both the sharpness of the resonance and the relative shift for a given Δn_p.
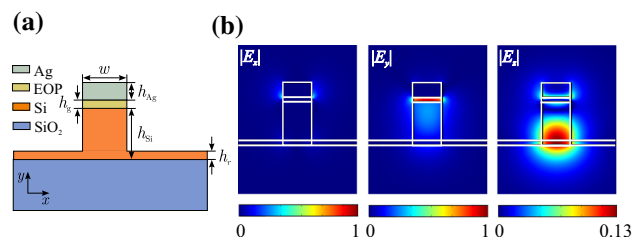
Fig. 8 a Cross section of the employed CGS bus waveguide and electric field profile of the TM excitation mode at $\lambda = 1.55$ µm
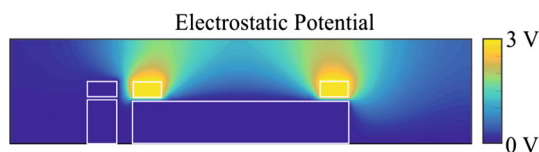
Before proceeding with further investigating the proposed hybrid plasmonic modulators, we employ the definition of the FoM to justify the selection of one important geometrical parameter, namely the thickness of the EOP layer h_g, which has been selected equal to 30 nm. Focusing on the case where $R_i = 0.75R_o$, we calculate the FoM of the resonator for different values of h_g by properly adjusting R_o such that $\lambda_r \simeq 1.55\,\mu m$. Figure 6 shows the dependence of the FoM on h_g. Clearly, in the extreme cases of $h_g \to 0$ or $h_g \to \infty$ the structure degenerates in a single Si/Ag plasmonic interface and a Si resonant microdisk, respectively, i.e., poorer resonators, characterized by low FoM values. At $h_g \sim 30$ nm the FoM is maximized, thus demonstrating that this particular selection is not arbitrary, but leads to the optimization of the resonator's performance.

2.2 Electro-optic modulation in micro-disk-ring resonators coupled with a conductor-gap-silicon plasmonic bus waveguide
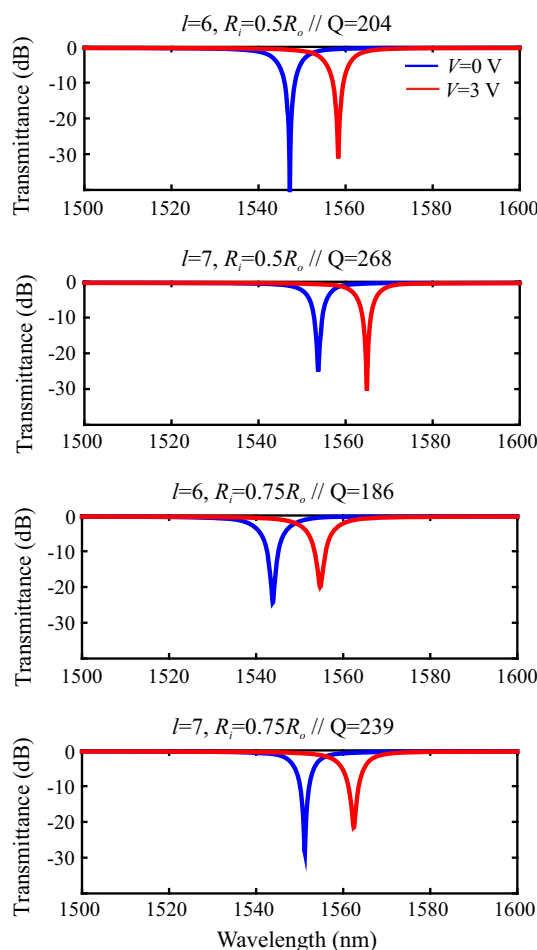
In this subsection, we investigate the resonator's properties in the context of the integrated hybrid plasmonic electro-optic modulator shown schematically in Fig. 7. The micro-ring-disk resonator is side-coupled to a CGS bus waveguide at a separation distance s. The total length of the device is equal to $L = 4R_o$. The RF voltage is applied between the silver cup of the microring and the grounded Si microdisk. The CGS waveguide with $w_{Si} = 200$ nm is excited by the plasmonic TM-mode whose electric field components are depicted in Fig. 8. The modal effective index at 1.55 μm equals $2.36 - j0.0023$, which corresponds to a propagation length $L_p = 53.4\,\mu m$, characteristic of CGS waveguides, as also experimentally verified [23]. The modal profile is typical of this type of waveguides; most of the electric field is confined in the thin EOP layer while a smaller part associated with the E_z component leaks toward the basis of the Si stripe.

The application of the RF voltage leads to a voltage drop and thus RF field intensity mainly in the EOP layer, owing to its small thickness h_g. Away from the edges of the microring, this electric field intensity can be fairly considered constant and equal to $E_s = V/h_g$. Nevertheless, in order to fully take into account the local spatial variations of the modulating field, we first rigorously calculate the electrostatic potential distribution, as in the example shown in Fig. 9, calculated for $V = 3$ V and plotted at the cross-section plane $z = L/2$. The Ag cup of the CGS waveguide is left at a floating potential, while the Si parts are grounded. The RF permittivities for silica and EOP are, respectively, equal to 3.9 and 2.6. The application of the bias voltage is also expected to induce an nm-thick free-carrier exponentially varying accumulation/depletion layer at the Si/EOP interface under the Ag cups, depending on the polarity of the driving field. In the case of FC accumulation, the local Si refractive index modulation would lead to a maximum increase in the imaginary index by approximately one order of magnitude at the Si/EOP interface [32]. This effect can be safely neglected, as simulations have shown that less than 0.1% of the optical energy of the resonant modes resides in the 5-nm-thick Si ring-shaped volume below the Si/EOP interface. Moreover, by properly selecting the dopant type and/or polarity of the poling field, a depletion layer can be instead induced, which would eliminate any relevant issues of extra optical losses in Si.

Fig. 9 Profile of the electro-static potential at the $z = L/2$ plane for a voltage $V = 3$ V applied between the microring silver cup and the grounded silicon as shown in Fig. 7
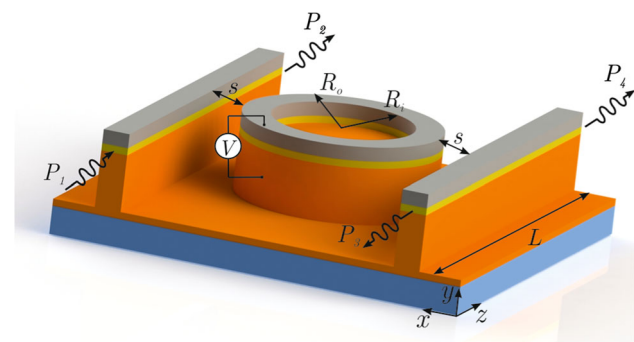

Fig. 10 Transmittance of the modulator in the rest ($V = 0$ V) and biased ($V = 3$ V) case for the four configurations under study

Table 1 Performance characteristics of the proposed hybrid plasmonic modulator

	IL_1 (dB)	ER_1 (dB)	IL_2 (dB)	ER_2 (dB)	C (fF)	E/bit (fJ)
$l = 6, 0.5R_o$	0.82	40.3	0.6	30.6	0.96	2.16
$l = 6, 0.75R_o$	0.92	23.3	0.71	19.3	0.56	1.26
$l = 7, 0.5R_o$	0.68	24.4	0.48	30	1.26	2.82
$l = 7, 0.75R_o$	0.84	27.7	0.67	20.8	0.73	1.65

Once the RF field profile has been calculated, the local modulation of the EOP index $\Delta n_p(\mathbf{r})$ is obtained and fed into the finite-element electromagnetic solver that studies the lightwave response of the system. The dispersion of silica, silicon, and Ag has been taken into account via the corresponding Sellmeier [33] and Drude [34] models. The modulator is excited by the hybrid plasmonic mode discussed in Fig. 8 and the power transmittance at the exit port is recorded for the rest and the biased case, assuming a maximum applied voltage $V = 3$ V. The separation distance has been selected such that critical coupling is achieved in the rest case, which is the condition that leads to minimum transmittance. For the $l = 6$ ($l = 7$) case, the optimal value of s was found equal to 100 nm (110 nm), by tuning it in steps of 5 nm. Theoretically, at the critical coupling regime the transmittance at λ_r is zero (infinite extinction ratio); however, due to fabrication issues and material constraints it is impossible to achieve in practice.

Figure 10 summarizes the spectral response of the modulator for all four cases under consideration. In the wavelength window of interest, namely between 1.5 and 1.6 nm, there is only one mode that can couple to the bus waveguide, whose properties have been discussed in Sect. 2.1. The quality factors of the resonances at the rest case are also reported. Higher Q values are obtained for larger external and smaller internal radii, at the expense of higher capacitance. In each scenario, there are two working wavelengths, corresponding to minimum transmittance at

either the rest or the biased case. In order to provide a comprehensive comparison, we summarize in Table 1 the performance characteristics of the modulator. The insertion losses (IL) and extinction ratio (ER) are reported for the first (rest) and second (biased) λ_r and the switching energy per bit has been calculated as $0.25CV^2$, which corresponds to a non-return-to-zero random bit sequence modulation.

As expected, there is a trade-off between insertion losses and capacitance or, equivalently, energy consumption. Owing to a slightly asymmetric shape of the transmittance spectrum, the second (longer) working wavelength exhibits somewhat lower insertion losses. In the $l = 6$, $R_i = 0.75R_o$ case, the switching energy is only 1.26 fJ/bit and by allowing for slightly higher IL, although still below 1 dB, the switching energy can drop below 1 fJ/bit by lowering the operating voltage correspondingly. These values are of the same order of magnitude compared to state-of-the-art SOH electro-optic [3] or silicon photonics modulators [35], while keeping the overall footprint of the device in the few square micron scale.

2.3 A 2×2 add-drop switching matrix

In this subsection, we preliminarily investigate the performance of the proposed modulator configured in a 2×2

Fig. 12 Transmittance of the 2×2 switch in the rest ($V = 0$ V) and biased ($V = 3$ V) case for $R_o = 695$ nm and $R_i = 0.75R_o$ and for two values of the separation s (100 and 40 nm)
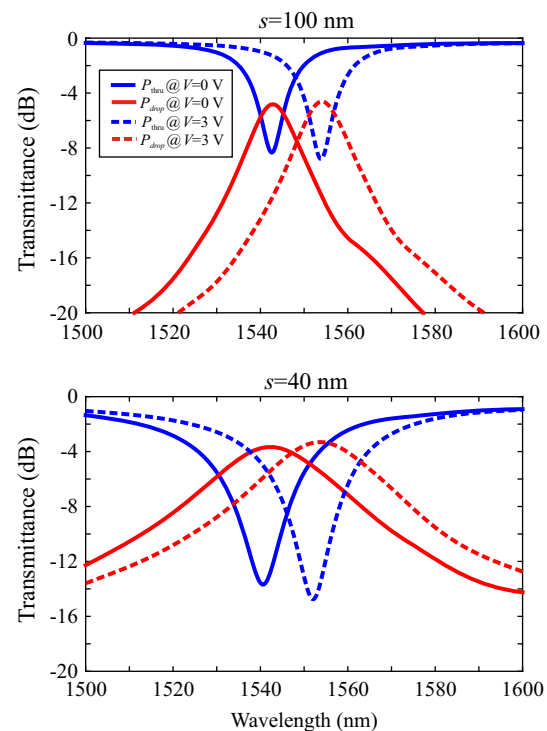
Fig. 11 Schematic layout of the 2×2 switch consisting of a micro-ring-disk resonator symmetrically placed between two CGS bus waveguides

Table 2 Performance characteristics of the proposed 2×2 hybrid plasmonic switching matrix

Port s (nm)	Thru 100	Drop 100	Thru 40	Drop 40
IL_1 (dB)	1.26	4.82	5.02	3.71
IL_2 (dB)	1.1	4.62	4.56	3.36
ER_1 (dB)	7.07	6.74	8.67	2.19
ER_2 (dB)	7.7	6.93	10.19	1.79

switching matrix, as depicted in Fig. 11. By side coupling the micro-ring-disk resonator with two CGS bus waveguides, a four-port device is formed. Following the notation of Fig. 11, the device is excited at Port #1 and Ports #2 and #3 are the through and drop ports, respectively. At the resonant wavelength, the transmittance of the through (drop) port is minimized (maximized) and the device can operate as a symmetric 2×2 switching matrix, provided that the separation gap is equal for both bus waveguides.

Figure 12 shows the transmittance spectra for the through and drop ports at both the rest and biased state for two values of the separation gap, namely 100 and 40 nm, calculated for the $l = 6$, $R_i = 0.75R_o$ scenario. The performance of the switch is summarized in Table 2, for both ports and separation values. The presence of the second bus waveguide introduces an additional channel for outcoupling the energy from the resonator, thus canceling the critical coupling condition for $s = 100$ nm, which was valid for the single-bus modulator. The extinction ratios obtained for both ports are moderate, around 7 dB, and the drop port suffers from higher insertion losses, which is a common feature in lossy resonating four-port devices. The extinction ratio for the through port can be improved by reducing the separation; however, this comes at the expense of poor ER for the drop port. Further investigation of this structure is in progress in order to find a favorable trade-off between the performance of the two ports.

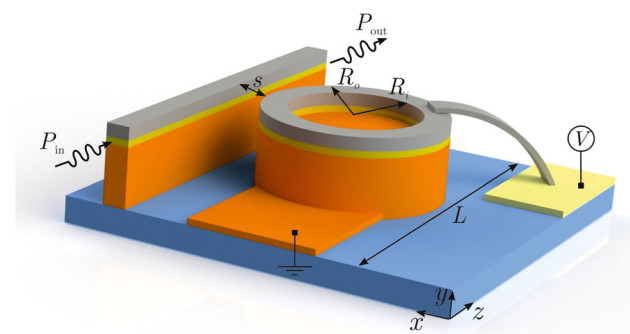In the results presented thus far we have considered that the silicon pad layer of thickness h_r is infinite, although this in general deteriorates the performance of the modulator by enabling some part of the energy to leak out of the silicon microdisk. In a realistic configuration, one might need to properly pattern only some parts in order to provide the necessary contacts for the RF connectorization of the resonator. One such configuration is schematically shown in Fig. 13. As discussed in [21], the modulation bandwidth of EOP hybrid plasmonic modulators is not limited by the almost instantaneous response of the polymer molecular polarizability, nor the photon lifetime in the optical resonant cavity, owing to the moderate quality factors, but rather by the RC time constant τ of the electrical connection circuit. In that context, the use of silicon/metallic pads and bridges, which have been employed in relevant experimental demonstrations [13], can lower the overall resistance of the RF circuit to a few KΩ, given also the low resistivity of the considered doped Si. It is stressed that in this work we have considered a Si-doping level of 10^{19} cm^{-3}, in order to induce a negligible FC dispersion effect. By optimizing the optical and electrical circuit design, higher doping concentrations could in principle reduce further the Si resistivity without severely compromising the performance of the device. Indicatively, by keeping the total resistance below 10 KΩ and given the very low capacitance of the proposed device, which is in the range of 1 fF, very high modulation speeds, above 100 GHz, are enabled.

3 Conclusions

In brief, we have studied a hybrid plasmonic modulator based on a silicon microdisk, plasmonic microring resonator enhanced with an electro-optic polymer, based on the conductor-gap-silicon platform. The proposed modulator features micron-scale footprints, operating voltages of a few Volt and provides large modulation depths with less than 1 dB insertion losses. More important, the per-bit energy needed to modulate the optical carrier is in the order of one femtojoule, thus rendering the modulator a promising solution in view of integrated plasmonic circuits for intrachip signal processing and communication.

Fig. 13 Schematic layout of a possible electrical connectorization pattern for the proposed electro-optic hybrid plasmonic modulators

References

1. D.K. Gramotnev, S.I. Bozhevolnyi, Nat. Photonics **4**, 83 (2010)
2. A. Emboras, C. Hoessbacher, C. Haffner, W. Heni, U. Koch, P. Ma, Y. Fedoryshyn, J. Niegemann, C. Hafner, J. Leuthold, IEEE J. Sel. Top. Quantum Electron. **21**, 6990493 (2015)
3. K. Liu, C.R. Ye, S. Khan, V.J. Sorger, Laser Photonics Rev. **9**, 172 (2015)
4. V.E. Babicheva, A. Boltasseva, A.V. Lavrinenko, Nanophotonics **4**, 165 (2015)
5. A. Melikyan, L. Alloatti, A. Muslija, D. Hillerkuss, P.C. Schindler, J. Li, R. Palmer, D. Korn, S. Muehlbrandt, D. Van

Thourhout, B. Chen, R. Dinu, M. Sommer, C. Koos, M. Kohl, W. Freude, J. Leuthold, Nat. Photonics **8**, 229 (2014)

6. A. Melikyan, K. Koehnle, M. Lauermann, R. Palmer, S. Koeber, S. Muehlbrandt, P.C. Schindler, D.L. Elder, S. Wolf, W. Heni, C. Haffner, Y. Fedoryshyn, D. Hillerkuss, M. Sommer, L.R. Dalton, D.V. Thourhout, W. Freude, M. Kohl, J. Leuthold, C. Koos, Opt. Express **23**, 9938 (2015)

7. D.C. Zografopoulos, R. Beccherelli, J. Opt. **15**, 055009 (2013)

8. D.C. Zografopoulos, R. Beccherelli, Opt. Express **21**, 8240 (2013)

9. D.C. Zografopoulos, R. Beccherelli, Plasmonics **8**, 599 (2013)

10. D. Korn, R. Palmer, H. Yu, P.C. Schindler, L. Alloatti, M. Baier, R. Schmogrow, W. Bogaerts, S.K. Selvaraja, G. Lepage, M. Pantouvaki, J.M.D. Wouters, P. Verheyen, J. Van Campenhout, B. Chen, R. Baets, P. Absil, R. Dinu, C. Koos, W. Freude, J. Leuthold, Opt. Express **21**, 13219 (2013)

11. S. Koeber, R. Palmer, M. Lauermann, W. Heni, D.L. Elder, D. Korn, M. Woessner, L. Alloatti, S. Koenig, P.C. Schindler, H. Yu, W. Bogaerts, L.R. Dalton, W. Freude, J. Leuthold, C. Koos, Light Sci. Appl. **4**, e255 (2015)

12. S. Randhawa, S. Lachèze, J. Renger, A. Bouhelier, R.E. de Lamaestre, A. Dereux, R. Quidant, Opt. Express **20**, 2354 (2012)

13. C. Haffner, W. Heni, Y. Fedoryshyn, J. Niegemann, A. Melikyan, D.L. Elder, B. Baeuerle, Y. Salamin, A. Josten, U. Koch, C. Hoessbacher, F. Ducry, L. Juchli, A. Emboras, D. Hillerkuss, M. Kohl, L.R. Dalton, C. Hafner, J. Leuthold, Nat. Photonics **9**, 525 (2015)

14. J.H. Zhu, X.G. Huang, X. Mei, Chin. Phys. Lett. **28**, 088501 (2011)

15. J.H. Zhu, X.G. Huang, X. Mei, Plasmonics **6**, 605 (2011)

16. X. Piao, S. Yu, N. Park, Opt. Express **20**, 18994 (2012)

17. X. Sun, L. Zhou, X. Li, Z. Hong, J. Chen, Appl. Opt. **50**, 3428 (2011)

18. M. Xu, F. Li, T. Wang, J. Wu, L. Lu, L. Zhou, Y. Su, J. Lightwave Technol. **31**, 1170 (2013)

19. D.C. Zografopoulos, L. Shahada, M.A. Swillam, R. Beccherelli, Appl. Phys. A **122**, 344 (2016)

20. F. Lou, D. Dai, L. Thylen, L. Wosinski, Opt. Express **21**, 20041 (2013)

21. D.C. Zografopoulos, M.A. Swillam, R. Beccherelli, IEEE Photon. Technol. Lett. **28**, 818 (2016)

22. A.O. Zaki, N.H. Fouad, D.C. Zografopoulos, R. Beccherelli, M.A. Swillam, Proc. SPIE **9744**, 97441K (2016)

23. M. Wu, Z. Han, V. Van, Opt. Express **18**, 11728 (2010)

24. D. Dai, Y. Shi, S. He, L. Wosinski, L. Thylen, Opt. Express **19**, 23671 (2011)

25. F. Lou, Z. Wang, D. Dai, L. Thylen, L. Wosinski, Appl. Phys. Lett. **100**, 241105 (2012)

26. F. Li, M. Xu, X. Hu, J. Wu, T. Wang, Y. Su, Opt. Commun. **286**, 166 (2013)

27. D.A. Ketzaki, O. Tsilipakos, T.V. Yioultsis, E.E. Kriezis, J. Appl. Phys. **114**, 113107 (2013)

28. A.K. Pitilakis, E.E. Kriezis, J. Opt. Soc. Am. B **30**, 1954 (2013)

29. C. Koos, J. Leuthold, W. Freude, M. Kohl, L. Dalton, W. Bogaerts, A.L. Giesecke, M. Lauermann, A. Melikyan, S. Koeber, S. Wolf, C. Weimann, S. Muehlbrandt, K. Koehnle, J. Pfeifle, W. Hartmann, Y. Kutuvantavida, S. Ummethala, R. Palmer, D. Korn, L. Alloatti, P.C. Schindler, D.L. Elder, T. Wahlbrink, J. Bolten, J. Lightwave Technol. **34**, 256 (2016)

30. K.M. Schulz, S. Prorok, D. Jalas, S.R. Marder, J. Luo, A.K.-Y. Jen, R. Zierold, K. Nielsch, M. Eich, Opt. Mater. Express **5**, 1653 (2015)

31. Commercial finite-element solver "COMSOL Multiphysics", ver. 5.1, Comsol Inc. (2015)

32. MOSCap, Metal-oxide-semiconductor junction simulation tool. https://nanohub.org

33. B. Tatian, Appl. Opt. **23**, 4477 (1984)

34. M.A. Ordal, R.J. Bell, J.R.W. Alexander, L.L. Long, M.R. Querry, Appl. Opt. **24**, 4493 (1985)

35. E. Timurdogan, C.M. Sorace-Agaskar, J. Sun, E.S. Hosseini, A. Biberman, M.R. Watts, Nat. Commun. **5**, 4008 (2014)